Enhancing the active motion of hematite microswimmers

Schyck, Sarah; Caipa Cure, Silvana A. ; Sacanna, Stefano; Rossi, Laura

DOI
10.1016/j.apmt.2025.102947

Publication date
2025

Document Version
Final published version

Published in
Applied Materials Today

Applied Materials Today 47 (2025) 102947

Contents lists available at ScienceDirect

Applied Materials Today

journal homepage: www.elsevier.com/locate/apmt

Enhancing the active motion of hematite microswimmers

Sarah Schyck [a,*], Silvana A. Caipa Cure [a,1], Stefano Sacanna [b], Laura Rossi [a]

[a] Department of Chemical Engineering, Delft University of Technology, Van der Maasweg 9, Delft, 2629HZ, The Netherlands
[b] Department of Chemistry, New York University, 29 Washington Place, New York, 10003, NY, USA

ARTICLE INFO

Dataset link: 10.4121/FE6B581D-6149-440D-8455-17CCE4E71F35.V1

Keywords:
Self-propelled particles
Photocatalysis
Hematite
Calcination
Mean-squared displacement (MSD)
Optical microscopy
Active motion

ABSTRACT

The demand for autonomous, self-propelled active particles is rapidly growing in soft matter research, driven by their potential applications in cargo delivery, environmental remediation, and as valuable models for understanding biological systems. Despite this interest, the challenge of designing highly active and cost-effective microparticles persists. Here, we present a simple and general method to enhance the photocatalytic performance of hematite microparticles through thermal treatment. By calcining the particles in air at 600 °C for varying durations, we achieve significant improvements in their light-driven motility. Optical microscopy tracking reveals up to an 87-fold increase in mean-squared displacement (MSD) at short lag times. Our findings highlight a simple and scalable method to substantially improve the efficiency of hematite microparticles, and this advancement opens new avenues for their application in key areas of soft matter and photocatalysis research.

1. Introduction

Active microswimmers are capable of navigating through complex, three-dimensional environments and have potential implications in drug delivery [1], environmental remediation [2–4], biomedical diagnostics [5], as well as models for collective phenomena and even scenarios such as the flight of unmanned aerial vehicles [6–8]. Several propulsion mechanisms are currently exploited for the design of active systems. One example involves propulsion driven by phoretic motion, which arises from the photocatalytic decomposition of fuel to produce self-generated chemical gradients.

A frequently used fuel is hydrogen peroxide, H_2O_2, whose decomposition into O_2 and H_2O is often catalyzed in the presence of illuminated semiconductors [9,10]. For the particles to propel, the self-generated gradients or the particles themselves must be asymmetric [1]. Therefore, numerous methods have been developed to produce active microswimmers with inherent asymmetry. Examples of such systems include: Janus particles [11,12] and bimetallic rods [13], which possess photocatalytic material on one-half of the particle. However, the complex synthetic strategies required to prepare these microparticles inhibit both applications and up-scaling.

Hematite, as a photocatalytic active swimmer, mitigates this limitation due to its scalability and spontaneous symmetry breaking required for active motion [14,15]. Hematite active swimmers also play an essential role in dynamic assembly and cargo transport [3,14,16,17] owing to their ability to transition between active and passive behavior and their inherent magnetic moment [18].

For photocatalysis, the semiconductor absorbs photons greater or equal to its band gap, and electrons from the valence band move to the conduction band. This process creates an electron–hole (e–h) pair that can either (i) recombine or (ii) diffuse to the surface and participate in redox reactions [19]. Hematite's short light penetration depth and fast e–h recombination time, limit its catalytic activity compared to other active particles, such as TiO_2 or Pt-based microswimmers [20]. For example, the light penetration depth of hematite at $\lambda = 550$ nm is ≈ 118 nm and ≈ 20 nm at $\lambda = 395$ nm [21]. Whereas the diffusion length of an e–h pair is only 2–4 nm, and the e–h recombination time is around 2 ps [19]. On the other hand, photoactive TiO_2 has an e–h pair diffusion length of 9.9 μm and a recombination time ≥ 50 ns depending on the crystal phase [22,23].

In this work, we investigate how calcination affects the photocatalytic motility of hematite microparticles to overcome some of hematite's limitations. Calcination, a process in which particles are heated to high temperatures, generally results in a more homogeneous material with less defects and surface impurities. For example, calcination is used to tune the internal crystal structure and crystallite size of TiO_2 particles, leading to an enhancement of the particles' photocatalytic properties [24]. For hematite nano-scale particles, this technique has proven effective in enhancing chemical degradation in environmental remediation [25]. For instance, the preparation of hematite

* Correspondence to: Faculty of Aerospace Engineering, Delft University of Technology, Kluyverweg 1, Delft, 2629HS, The Netherlands.
E-mail address: s.n.schyck@tudelft.nl (S. Schyck).
[1] Present Address: Soft Matter Physics, Huygens-Kamerlingh Onnes Laboratory, Leiden University, P.O. Box 9504, Leiden, 2300 RA, The Netherlands.

https://doi.org/10.1016/j.apmt.2025.102947
Received 29 July 2025; Received in revised form 30 September 2025; Accepted 2 October 2025
Available online 10 October 2025

nanostructures with a calcination step showed a higher degradation efficiency for dye molecules [26], pharmaceutical waste molecules [27], and even coal combustion waste [28].

Additionally, calcined hematite nanoparticles have shown enhanced electrocatalysis when acting as an anode material for lithium-ion batteries [29]. Thus, calcination, a simple step after the synthesis of hematite microparticles, may be a viable pathway to enhance hematite's photocatalytic properties and, therefore, its active behavior, without resorting to chemical modifications. In this work, we explored the active motion of photocatalytic hematite particles using hydrogen peroxide as a fuel. We investigated non-calcined hematite microswimmers alongside calcined microswimmers exposed to UV wavelengths. Non-calcined microswimmers perform noticeably worse than all calcined microswimmers with the best-performing microswimmers reaching an average 87-fold increase in their mean-squared displacements.

2. Methods

2.1. Particle preparation

Hematite superballs were prepared from a modified gel–sol synthesis [30], and details on the preparation procedure can be found in a previous work [31]. Briefly, a 90 mL 6 M NaOH solution is slowly added to a 100 mL 2 M aqueous iron chloride solution to form a gel–sol that is aged at 100 °C for 8 days. Hematite samples were calcined in a Nabertherm L5/S27 furnace in air at 600 °C for 2, 3, and 10 h in a ceramic crucible. An initial ramp-up over 1.5 h of 6.5 degrees per minute was used for all samples. After calcination, the furnace automatically stopped heating and slowly cooled to room temperature. Powdered calcined samples were loosen from the crucible by gentle scraping with a metal spatula and redispersed into water with 0.002 wt% of tetramethylammonium hydroxide (TMAH), to stabilize the particle suspension, via an ultrasonic bath.

2.2. Particle characterization

2.2.1. Morphology

Visualization of hematite particles was done with a scanning electron microscope (JEOL-6010) and an atomic force microscope (Bruker Dimension Icon). Atomic Force Microscopy (AFM) image analysis was performed with open source python packages, specifically SPIEpy [32] and pySPM [33].

2.2.2. Light absorption

Light absorption properties of samples were investigated using a UV–Vis spectrometer (Perkin Elmer UV/VIS/NIR Lambda 1050) equipped with a mini-integrating sphere (150 mm InGaAs) for diffuse reflectance measurements. Band gap energies were calculated via the Kubelka–Munk method: $(f(R)h\nu)^{\gamma} = A(h\nu - E_g)$ where $f(R) = \frac{(1-R)^2}{2R}$, R is the measured reflectance, $h\nu$ is the photon energy, E_g is the band gap, A is a proportionality constant, and γ is 2 for the direct allowed transition type of hematite corresponding to the hybridization between O 2p and Fe 3d states [34]. The linear region of the Tauc plots, $(f(R)h\nu)^{\gamma}$ plotted against $h\nu$, are fit and E_g is extracted from the x-intercept of the linear fits [35].

2.2.3. Crystallinity

Single particle X-ray diffraction (XRD) on single particles was preformed at the ID13 beamline of the European Synchrotron Radiation Facility (ESRF) in Grenoble, France. Samples of calcined hematite were prepared on silicon nitride windows via a droplet deposition. The incident X-ray beam with a photon energy of 13 keV (0.954 Å) and size of 250 nm was focused on a Dectris Eiger X 4M detector (2048 × 2048 pixels with pixel size of 75 μm) that was positioned 76 mm from the sample. 2D scattering patterns were collected with resolution up to $2\theta = 55$, i.e., $d = 1.0$ Å for several particles to account for various orientations of the particles on the substrate. Sample rotation was performed from +45° to −45°. Data analysis and 2D integration of diffraction data was done in python with the PyFai package [36]. We probed how the crystallite size changed for the various planes via Scherrer's equation: $D_{hkl} = K\lambda/\beta\cos\theta$ [37]. The measured crystallite size is limited to the resolution of the experimental set-up which was determined via calibration with Al_2O_3 to be 200 nm. Therefore, crystallite sizes > 200 nm are reported to be ≥ 200 nm.

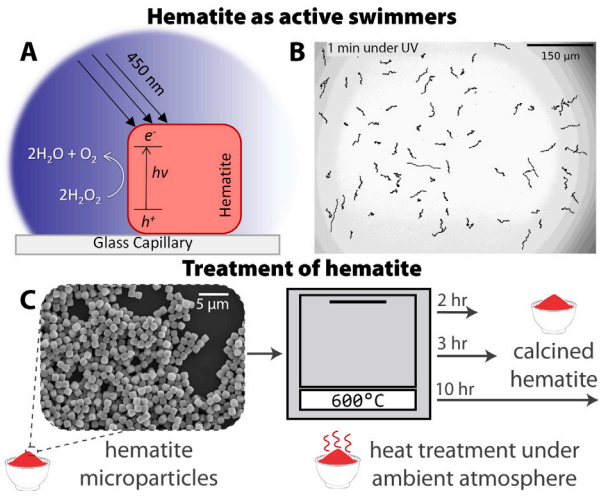

Fig. 1. Active motion and heat treatment of hematite microparticles. (A) Schematic of photocatalytic propulsion: under 450 nm illumination, hematite microparticles decompose fuel at their surface, generating motion along the inner surface of a glass capillary. (B) Bright field microscopy video still of a hematite microparticle swimming along a glass capillary. Superimposed black tracks indicate particle trajectories. (C) Outline of the thermal treatment procedure. SEM image (left) of hematite microparticles which are shown in the schematic (right) placed in a furnace under ambient air and calcined at 600 °C for 2, 3, or 10 h.

2.3. Active motion characterization

Aqueous swimming dispersions contained 0.00075 wt% hematite particles and 5 wt% H_2O_2 and were adjusted to pH 9 by drop-wise addition of 1 wt% TMAH. Samples were collected inside flat rectangular capillaries (Vitrocom 0.05 × 1.00 mm) and sealed with wax on a microscope slide. We followed the particle dynamics via an inverted microscope (Zeiss Axio Observer) equipped with a 20x objective (N-Achroplan 20x/0.45 M27), a CCD camera (Axiocam 705 color), and a mercury lamp (HXP 120 V). The intensity of the light source was controlled via a manual knob, and a longpass filter (AT450/50x) was used to restrict light emission to 425–475 nm at 2.4 mW. We acquired time lapses with frame rates between 2 and 55 fps for up to 2 minutes. The particles' positions were followed over time and their mean-squared displacements (MSD) were calculated in Python with the TrackPy package [38]. We collected > 100 particle trajectories by imaging several areas in the same capillary for each sample.

3. Results and discussion

The observed swimming behavior of hematite microparticles arises from self-phoretic propulsion, driven by asymmetric chemical gradients that form as hydrogen peroxide (H_2O_2) is decomposed at the particle surface under illumination [9]. As depicted in Fig. 1A, the photocatalytic activity of hematite is activated under 450 nm light, leading to localized fuel consumption and the generation of chemical gradients in the surrounding solution. While the entire particle surface may participate in this reaction, directional propulsion typically emerges

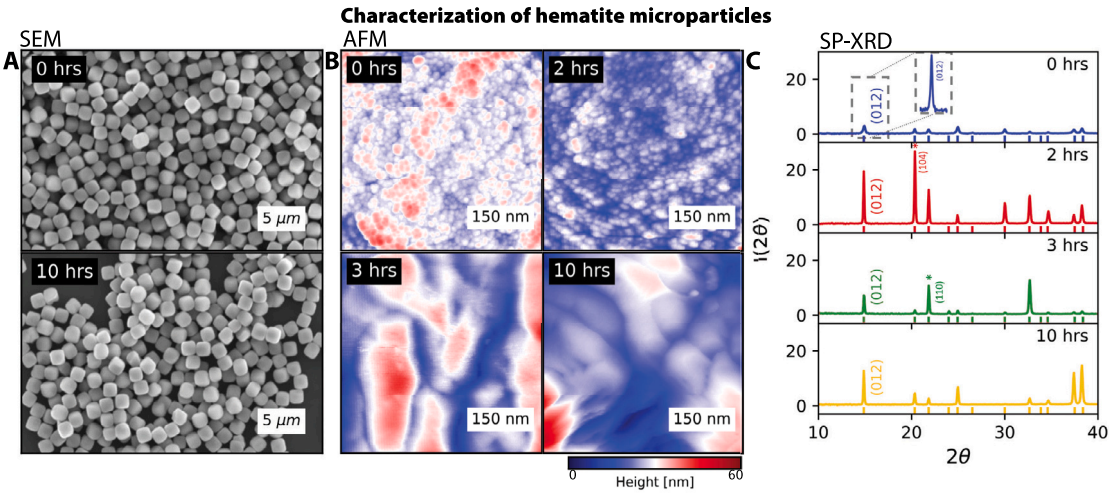

Fig. 2. Characterization of treated hematite. (A) SEM images of non-calcined (0 h) and calcined for 10 h hematite microparticles. (B) AFM images of a 500 × 500 nm surface of hematite superballs non-calcined (0 h) and calcined for 2, 3, and 10 h. (C) Single particle XRD patterns for hematite samples of 0, 2, 3, and 10 h of calcination 600 °C. Straight vertical lines represent peak positions for bulk hematite.

due to spontaneous symmetry breaking. This can originate from surface irregularities, contact with a nearby substrate, or fluctuations in the reaction field, resulting in net motion along the capillary surface [14, 39].

To observe and quantify this motion, we suspend hematite microparticles in aqueous H_2O_2 solution within rectangular glass capillaries, which provide a confined environment suitable for tracking two-dimensional particle motion. The sample is uniformly illuminated with a 450 nm LED source to initiate photocatalytic propulsion. Videos of the particle dynamics are recorded from below using an inverted optical microscope equipped with a high-speed camera, enabling detailed analysis of individual particle trajectories. A representative video still from **Supplementary Video S1** is shown in Fig. 1B, illustrating a typical experiment in which particle trajectories are visualized as superimposed black traces. These traces depict the motion of particles propelling along the surface of a glass capillary under UV illumination.

To evaluate how heat treatment affects propulsion behavior, we subjected hematite microparticles to thermal calcination in ambient air at 600 °C for varying durations: 2, 3, and 10 h. The procedure is outlined schematically in Fig. 1C. Calcination is expected to alter key physical and chemical properties of the particles, including their crystallinity, surface roughness, and catalytic activity. These factors, in turn, may influence both the efficiency and character of self-phoretic propulsion. By systematically varying the calcination time, we aim to identify how such modifications impact microswimmer behavior and assess the potential of thermal treatment as a tuning mechanism for active colloidal systems.

3.1. Characterization of hematite microparticles

In order to investigate the effects of calcination on the active motion of hematite microswimmers, we subjected hematite superball particles to calcination at 600 °C for 2, 3, and 10 h. We further examined the superball morphology during different calcination steps through scanning electron microscopy (SEM) imaging and atomic force microscopy (AFM) measurements. Fig. 2A depicts SEM images before (0 h) and after (10 h) calcination of the hematite particles. We observed that the particle size and shape remained consistent during calcination where the particles' edge length was 1.4 μm with a dispersity of 4%.

To explore the surface morphology, we preformed AFM on 500 × 500 nm regions on the faces of individual particles, as illustrated in Fig. 2B. The AFM imaging of non-calcined particles (0 h) exhibited the presence of small nodules measuring approximately 15 ± 3 nm in diameter, which protruded to an average height of 21 ± 4 nm. Following a 2-hour calcination period, comparable nodules were observed distributed across the surfaces of the particles. However, a significant transformation took place on the particles' surface after 3 and 10 h of calcination, leading to the disappearance of the nodular features and the emergence of extensive uniform regions spanning across the surface. The height disparity between the lower valleys and surface peaks doubled, escalating from 32 nm to 68 nm. Although we observe slight morphological changes in the roughness after calcination, they are not as pronounced as in other hematite systems, where, for example, hematite platelets sinter into cubic particles [40].

The crystalline nature of the hematite samples prepared in this study was assessed through Single-Particle X-ray Diffraction (SP-XRD) measurements. Fig. 2C presents the XRD patterns of various calcined hematite samples. The resolved diffraction peaks align with the typical α-Fe2O3 $R\bar{3}c$ lattice (indicated by vertical lines) and exhibit lattice parameters of $a = b = 5.035$ Å [41]. For the non-calcined particles, the intensity, $I(2\theta)$, is relatively low, with $I_{max} = 2.94$ for the (012) *hkl* reflection indicated by the inset, in comparison to their calcined counterparts. This effect can be attributed to an increasing crystallite size and decreasing micro-strain after calcination [37].

Furthermore, we observed variations in the dominant reflection between particles. For instance, the particle calcined for 2 h exhibits a dominant (104) reflection, whereas the particle calcined for 3 h shows a dominant (110) reflection, as indicated by the starred peaks. This observation suggests the presence of preferential orientations in the crystal structure of hematite superballs, as reported by Sugimoto et al. [30], which depends on the superball position in the X-ray beam as described in **Supplementary Figure S1**.

For hematite superballs, it is expected that the {012} plane family encompasses the superball faces [42]. Thus, the crystallite size of the (012) reflections at different calcination times can be assessed by analyzing the (012) peak widths, β_{012}, using Scherrer's equation [37]. To obtain the average crystallite size for these planes, we analyzed the (012) peaks of four particles per sample.

For the non-calcined superballs (0 h), we observed an average crystallite size of 25 ± 1 nm, which is in good agreement with the previously reported crystallite size of the (012) plane of hematite superballs at 25.5 nm [42]. In all calcined samples, we observed a significant increase in crystallite size for all measured particles, with values reaching greater than the limit our experimental setup of ≥ 200 nm. Additionally, we observed an increase in crystallite size for the other crystallographic planes, see **Supplementary Figure S1**.

Since hematite superballs are faceted by the {012} family [42], we expect these planes to have a strong influence on their photocatalytic properties. Studies on the photocatalytic activity of faceted hematite had suggested that altering the shape of hematite to promote co-faceted particles, as is the case with bipyramidal hematite [43], may further enhance the photocatalytic activity [44]. Interestingly, studies on the photocatalytic degradation of organic molecules using hematite nanoparticles have suggested that smaller crystallite and particle sizes enhance photocatalytic activity [27,45,46]. Nevertheless, these studies already involved a calcination step of at least 150 °C before measurement, and the nanoparticle size and crystallite size varied from 8–100 nm. In the case of tungsten oxide microparticles, Nandiyanto et al. [47] demonstrated that increasing the crystallite size from 19–42 nm while maintaining the same particle size substantially enhanced the photocatalytic performance of tungsten oxide microparticles in a photo-degradation test of curcumin. This finding may provide a more accurate representation of our (micro-)hematite superball system.

To investigate changes in the optical properties after calcination, we conducted UV–Vis diffuse reflectance spectroscopy (DRS) measurements on both calcined and non-calcined hematite superballs (see **Supplementary Figure S2**). By applying the Kubelka–Munk formula, we estimated the band gap energy, E_g, of the two samples to be 2.05 eV and 1.85 eV for 0 h and 10 h of calcination time, respectively. Similar studies on hematite particles have demonstrated a consistent trend of decreasing band gap with increasing calcination temperature [27].

3.2. Active and Brownian motion of hematite swimmers

We first investigate dispersions of non-treated hematite superballs in an aqueous solution of H_2O_2 for their active and passive motion. Fig. 3A shows trajectories of the microswimmers from a common origin in the absence (red lines) and presence (black lines) of UV light. When the light is off, typical 2D Brownian trajectories. When the UV light is switched on, the micro-swimmers propel in various directions, characterized by relatively long and linear trajectories. The absence of a preferred directionality over the trajectories suggests that the swimming motion is primarily driven by the activity of hematite rather than influenced by external factors such as magnetic fields or fluid flows.

The dynamics of our hematite superballs is further investigated by calculating the time-averaged mean-squared displacement (TAMSD) and the ensemble mean-squared displacement (MSD) curves of the particles. For single-particle dynamics, the TAMSD is defined as

$$\overline{\delta^2(n)} = \frac{1}{N-n}\sum_{i=1}^{N-n}(\vec{r}_{i+n} - \vec{r}_i)^2 \tag{1}$$

where N is the total number of recorded frames, n is the lag in frames, and $\vec{r}_i$ is the particle position at frame i. To investigate the full sample, we employ the ensemble MSD, defined as

$$\langle \Delta r^2 \rangle = \langle (\vec{r}(t+\Delta t) - \vec{r}(t))^2 \rangle \tag{2}$$

where $\vec{r}(t)$ is the position of a particle at time t. Ensemble MSD's are calculated by averaging over several hundred particles. In the absence of UV light, as shown in Fig. 3B, the hematite particles display typical diffusive, linear MSD behavior which can be described by $\langle \Delta r^2 \rangle = 4D_0\Delta t$ where D_0 is the translational diffusion coefficient of the particle. In the presence of UV light, the particles exhibit characteristic active motion from their MSD profiles as shown in Fig. 3C. The MSD for this type of motion in 2D at any time is described by the Ornstein–Uhlenbeck equation [48] which is often reduced into three time lag, Δt, dependent regimes described by [49]:

$$\Delta t \ll \tau_r;\ \langle \Delta r^2 \rangle = 4D_0\Delta t$$
$$\Delta t \approx \tau_r;\ \langle \Delta r^2 \rangle = 4D_0\Delta t + 2v^2\Delta t^2$$
$$\Delta t \gg \tau_r;\ \langle \Delta r^2 \rangle = 4D_0\Delta t + 2v^2\tau_r\Delta t.$$

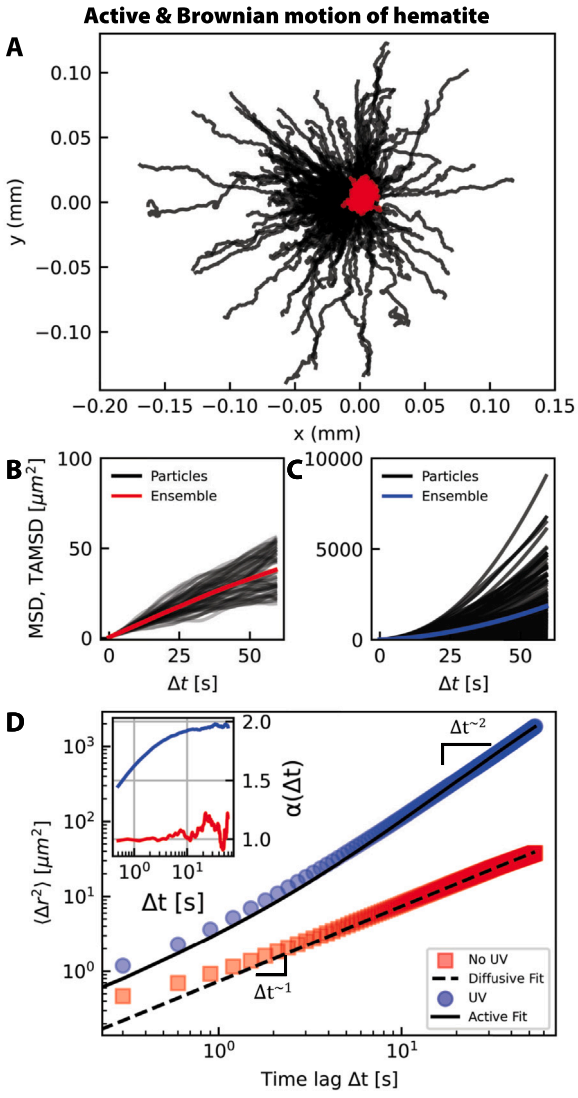

Fig. 3. Active and Brownian motion of hematite microparticles. (A) Overlaid trajectory plots for non-calcined hematite microparticles tracked over 60 s in the absence (red) and presence (black) of UV light, displayed from a common origin. (B,C) Mean-squared displacement (MSD) curves of individual particles (black lines) without (B) and with (C) UV illumination, along with the corresponding ensemble MSD curves. (D) Ensemble MSD curves for microswimmers without (red squares) and with (blue circles) UV light. Theoretical fits for Brownian diffusion and active motion are shown as dashed and solid lines, respectively. The inset depicts the time-local MSD-scaling parameter, $\alpha(\Delta t)$ for each MSD curve, no-UV and UV as red and blue lines, respectively.

In the first regime, at short time scales ($\Delta t \ll \tau_r$), the equation is reduced to the typical MSD for diffusive motion. In the second regime, when $\Delta t \approx \tau_r$, there is an additional second-order polynomial term due to the self-propulsion of the microswimmers. In the final regime, where $\Delta t \gg \tau_r$, rotational diffusion randomizes the direction of propulsion, leading again to diffusive behavior.

Therefore, we can identify the accessible dynamics regimes from the slope of the MSD curves on a log–log scale [50]:

$$\langle \Delta r^2(\Delta t) \rangle \propto (\Delta t)^{\alpha}.$$

Here, $\alpha = 1$ corresponds to normal Brownian motion, $\alpha < 1$ indicates subdiffusion (trapped-like motion), $\alpha > 1$ indicates superdiffusion (active motion), and $\alpha = 2$ corresponds to ballistic motion. Since the scaling exponent can vary with lag time, we calculate the time-local

scaling exponent from the MSD

$$\alpha(\Delta t) = \frac{\delta \log\langle \Delta r^2(\Delta t)\rangle}{\delta \log \Delta t}. \quad (3)$$

In Fig. 3D, for particles without UV light (red squares), we observe a clear linear behavior of the ensemble MSD with $\alpha \sim 1$. A fit to this linear region gives a diffusion coefficient of $D_0 = 0.182$ μm^2/s with an R^2 value of 0.998. The inset of Fig. 3D shows $\alpha(\Delta t)$, which remains around 1, corresponding to the expected diffusive motion.

For microswimmers under UV exposure, we observe only superdiffusive behavior, with $\alpha(\Delta t) > 1$, indicating that the experimental time resolution Δt_{Exp} is comparable to the rotational persistence time τ_r. For a spherical particle, the rotational time τ_r can be calculated using the Stokes relationship as $\tau_{\mathrm{r,sphere}} \approx 6$ s. In these experiments, we measured time lags of up to $\Delta t = 60$ s. This indicates that $\tau_r \geq 60$ s for the hematite superballs. The large τ_r paired with the observed linear trajectories during active motion may be related to the shape of the particles. Similarly, recent simulations of cubic micro-swimmers in micro-channels show that active cubes have linear trajectories inside micro-channels rather than the typical oscillatory behavior seen in spheres and ellipsoids [51].

To assess trajectory reproducibility, we calculated the ergodicity breaking (EB) parameter [52] defined by $EB(\Delta) = \langle(\overline{\delta^2(n)})^2\rangle / \langle\overline{\delta^2(n)}\rangle^2 - 1$ (see Supplementary Figure S3). While Brownian particles show EB $\approx$ 0 at short lag times (as expected), UV-activated particles remain nonergodic across all lag times, reflecting variability in swimming speeds and reorientation. Similar EB analyses have been applied to anomalous-diffusion models such as fractional Brownian motion with inertia, where massive particles lead to apparent nonergodicity [53].

To quantify the persistence of motion, we computed the mean first passage time (MFPT) [54] of the hematite microparticles to reach a threshold displacement of 10 μm. Particles without UV illumination exhibited an MFPT of 9.1±6.2 s, whereas UV-illuminated particles reached the same distance faster, with an MFPT of 3.9 ± 4.0 s. This behavior is also observed at larger threshold distances (**see Supplementary Figure S4**). This reduction reflects the enhanced active motion under UV exposure. The spread of MFPT values further indicates that active particles move more coherently, consistent with ballistic-like trajectories at short times.

3.3. Active motion after calcination

To understand the effect of calcination, we measured trajectories over the different calcination times as well as non-calcined particles indicated as 0 h shown in Fig. 4A. Hematite calcined for 2 h at 600 °C already changes the average trajectory length to 151 μm from the 45 μm for non-calcined hematite after 60 s. After 3 to 10 h of calcination, the average length of the particles' trajectories increases again up to 260 μm, apparent from the long trajectories extending farther than particles calcined for 2 h in Fig. 4A.

While most of the particle trajectories follow a relatively straight path, some trajectories appear to suddenly turn and change direction, as shown clearly in **Supplementary Figure S5**. The origin of these trajectory changes is due to the particle's inherent magnetic moment and subsequent dipole–dipole interactions where in one case they are repulsive and in the other attractive [55]. Therefore, when two particles approach each other, they will experience attraction or repulsion based on their respective (dipole) orientation which results in particle tracks with sharp deflections.

To minimize the effects of particle–particle interactions during our measurements, we prepared dilute dispersions (0.00075 wt%) of the particles in capillaries. During tracking analysis, trajectories of particles that form clusters are discarded, identified by instances where one particle's trajectory merges with another. In contrast, particles that only undergo brief deflections upon encountering others are retained in the analysis. Since the particles' trajectories span all angles from the origin, we assume that the influence of external magnetic fields, within the microscope's field of view, is negligible.

Fig. 4B shows the ensemble MSD curves as a function of the time lag for the samples with different calcination times. For all plots, the y-axis is scaled to 150,000 μm^2. For the MSD curves of non-calcined particles, denoted as 0 h, the particles still have characteristic active curves which can reach up to 1400 μm^2 at $\Delta t = 60$ s. After two hours of calcination at 600 °C, the MSD increases slightly while after 3 and 10 h of calcination the MSD increases greatly within the observed Δt, where 3 h of calcination results in a ensemble MSD curve greater at all time lags than the other particles.

In order to better compare samples with various calcination times, we extracted the MSD value at $\Delta t = 60$ s and 30 s in Fig. 4C. We visualize the data in the form of a violin plot on a logarithmic scale to account for broad distributions. Each violin-half in the plot shows in the horizontal axis the probability density for each TAMSD value at either a time lag of $\Delta t = 60$ s and 30 s. At $\Delta t = 30$ s, we see the same trend from the MSD curves where the non-calcined particles exhibit lower TAMSD values than their calcined counterparts, such that $\delta^2(\Delta t = 30\ s) \approx 20$ μm^2. After two hours of calcination, the median increases to $\approx$ 2000 μm^2, a hundred-fold increase. At $\Delta t = 60$ s, the calcination improves the average for samples by at least 20-fold as seen already for 2 h of calcination at $\Delta t = 60$ s. At 3 h of calcination time, we observed the highest obtained average TAMSD of 11,000 μm^2 or an average 87-fold increase at $\Delta t = 60$ s. A further increase in calcination time to 10 h leads to a lower average TAMSD (7,000 μm^2 at $\Delta t = 60$ s) with a larger spread of values.

We extracted the mean first passage time (MFPT) for particles with varying calcination times, considering passage distances up to 30 μm, shown in Fig. 4D. Consistent with the ensemble MSD curves and their time-local scaling exponents $\alpha(\Delta t)$, we find that the non-calcined particles (0 h) exhibit significantly higher passage times, with a nonlinear dependence on distance that persists until larger scales, again reflecting their super-diffusive behavior. In contrast, all calcined particles display an almost linear MFPT–distance relation, characteristic of typical ballistic motion. Among all samples, the particles calcined for 3 h show the lowest MFPT across the range, outperforming the other samples, suggesting that a calcination time of 3 h yields optimal performance. After 3 h, we also observed notable changes in surface morphology after 3 h of calcination and an increase in crystallite size (> 200 nm) for all calcined samples (Section 3.1). The observed structural modifications may relate to the observed enhancement in motility. Similar observations have been reported in related catalytic systems of hematite and CeO_2, where intermediate processing conditions create a "sweet spot" in activity [27,28,56]. In those cases, the speculate that surface oxygen vacancies are generated at optimal calcination temperatures and times, enhancing catalytic performance, while excessively high temperatures or prolonged treatment reduce defect density and thereby diminish activity.

To further support these findings, we extracted the propulsion velocities of individual microparticles by fitting their TAMSD curves to the model equation $\langle \Delta r^2 \rangle = 4D_0\Delta t + 2v^2\Delta t^2$, which accounts for both Brownian diffusion and ballistic self-propulsion. To isolate the self-propulsion contribution, we fixed the diffusion coefficient D_0 to the value obtained from Brownian motion in the absence of UV illumination ($D_0 = 0.182$ μm^2/s), ensuring consistency across all fits. The resulting velocities from these fits are summarized in Fig. 4E.

For untreated hematite microparticles, we obtained an average swimming velocity of 0.17 ± 0.06 μm/s. Upon calcination, the particles exhibited significant enhancements in motility. Specifically, particles calcined for 2, 3, and 10 h showed average velocities of 0.8 ± 0.4, 1.6 ± 0.9, and 1.16 ± 0.9 μm/s, respectively, corresponding to approximately 5-, 10-, and 7-fold increases relative to the untreated condition. This trend suggests that thermal treatment alters the structural or surface properties of the hematite in ways that facilitate more efficient catalytic

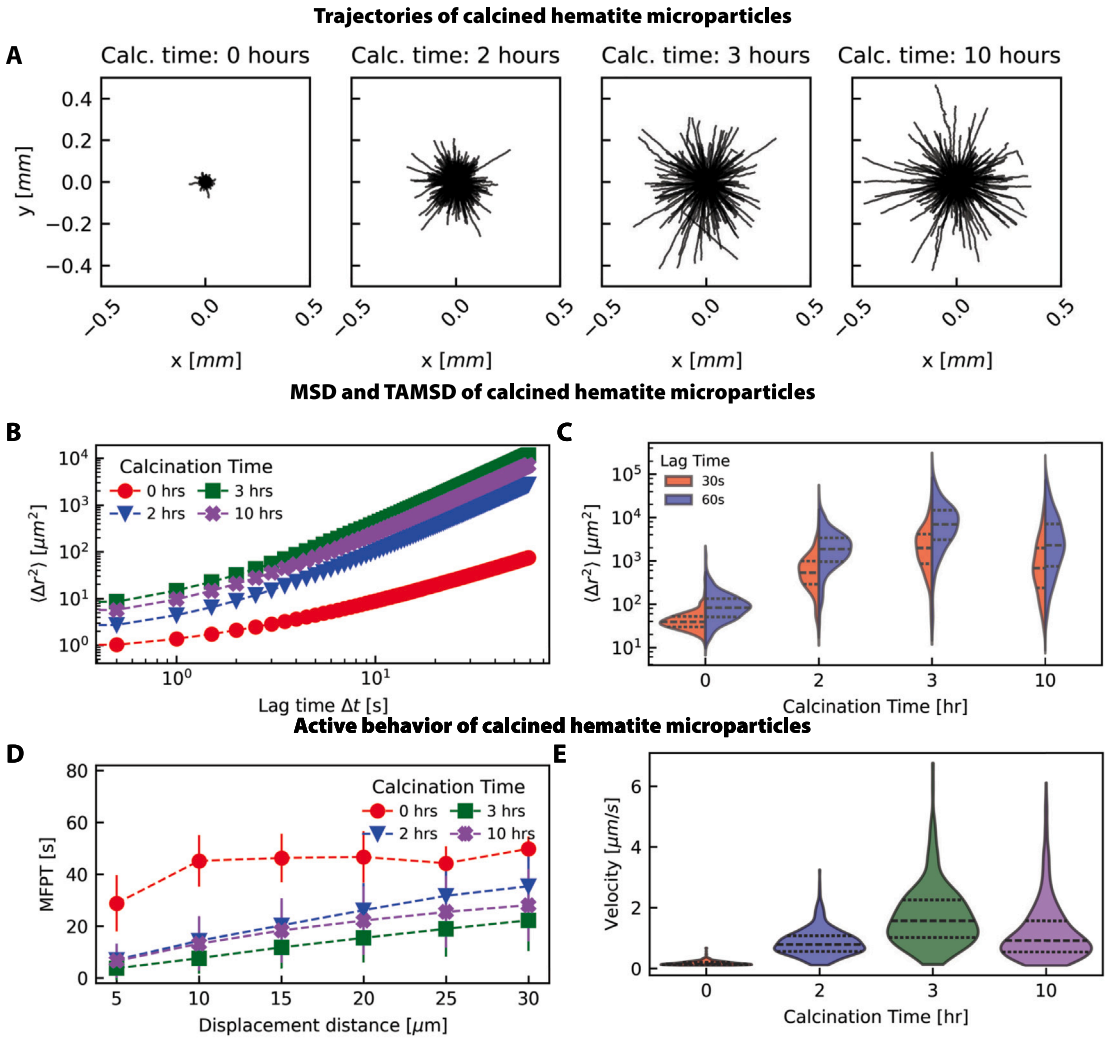

Fig. 4. Active motion behavior of hematite microparticles in the presence of H_2O_2 fuel and UV irradiation. (A) Particle trajectories originating from a common point over 1 min for non-calcined particles (0 h) and particles calcined at 600 °C for 2, 3, and 10 h. (B) Ensemble MSD curves for the same samples. (C) Violin plots of MSD at a lag time Δt = 60 s and 30 s, displayed on a logarithmic y-axis. (D) The MFPT of the particles at different set distances (symbols) with the standard deviation as the y-error. Dashed lines are added as a guide to the eye. (E) Extracted particle velocities (μ m/s) derived from MSD fitting. Dashed lines within the violin plots represent the median and quartiles.

decomposition of the hydrogen peroxide fuel, thereby increasing the strength of the chemical gradients driving self-phoretic propulsion.

The absolute velocities observed here are lower than those reported for microswimmer systems employing platinum or titanium catalysts. Such systems can reach speeds of 17 μm/s for TiO_2-based microswimmers at comparable fuel concentrations but under higher light intensities (9.7 mW compared to our 2.4 mW) [4,12]. It is well established that increasing light intensity enhances performance, as also previously shown for hematite microswimmers [14]. Our results therefore highlight the viability of hematite as a low-cost, earth-abundant alternative, especially since TiO_2 or Janus-based systems often require complex, multi-step fabrication processes. Furthermore, the ability to modulate swimming speed through simple furnace-based calcination introduces a tunable parameter for engineering microswimmer performance. These findings highlight the importance of post-synthesis treatment in tailoring particle behavior, and open new possibilities for designing responsive or adaptive microscale systems.

4. Conclusion

In this study, we explored the impact of calcination time on the photocatalytically driven active motion of micron-sized hematite superballs. Our results demonstrate that a minimum calcination time of 2 h at 600 °C already leads to a significant improvement in the observed active motion, with an average 20-fold increase in the mean square displacement (MSD) compared to non-calcined superballs. Notably, this improvement can be further enhanced to an impressive 87-fold increase when calcination is extended to 3 h at 600 °C. However, further extending the calcination to 10 h slightly reduces this enhancement, resulting in a 55-fold increase. These substantial enhancements in active motion are accompanied by changes in the optical band gap and crystallinity of the hematite particles, while the overall particle morphology remains unaffected. This work opens the door to using hematite microswimmers in more demanding soft matter systems, such as dynamic self-assembly, programmable cargo delivery, or real-time environmental sensing, where higher propulsion speeds are crucial. More broadly, these results suggest that post-synthetic thermal treatments could become a valuable tool for engineering next-generation active materials from earth-abundant semiconductors.

CRediT authorship contribution statement

Sarah Schyck: Writing – original draft, Methodology, Investigation, Formal analysis. **Silvana A. Caipa Cure:** Validation, Investigation. **Stefano Sacanna:** Writing – review & editing, Supervision. **Laura Rossi:** Writing – review & editing, Supervision, Resources, Conceptualization.

Funding

Stefano Sacanna was supported by the U.S. Department of Energy under grant number DE-SC-0020976.

Declaration of competing interest

The authors declare the following financial interests/personal relationships which may be considered as potential competing interests: Stefano Sacanna reports financial support was provided by U.S. Department of Energy. If there are other authors, they declare that they have no known competing financial interests or personal relationships that could have appeared to influence the work reported in this paper.

Acknowledgments

We would like to thank TUDelft's OM Group at for access to the furnace for particle calcination and DRS measurements, and Marcel Bus for assistance with the AFM measurements. We would also like to thank Asma Medjahed and Manfred Burghammer from the ID13 beamline at the ESRF for assistance with single particle diffraction experiments as well as Stefanie Neuber and Andrei Petukhov for assistance with analysis of X-ray experiments.

Appendix A. Supplementary data

Supplementary material related to this article can be found online at https://doi.org/10.1016/j.apmt.2025.102947.

Data availability

The data that support the findings of this study are openly available in 4TU.ResearchData at DOI: 10.4121/FE6B581D-6149-440D-8455-17CCE4E71F35.V1, reference number [57].

References

[1] S. Debata, N. Alam Kherani, S. Kumar Panda, D. Pratap Singh, Light-driven microrobots: capture and transport of bacteria and microparticles in a fluid medium, J. Mater. Chem. B 10 (40) (2022) 8235–8243.
[2] S.H. Sajjadi, E.K. Goharshadi, Highly monodispersed hematite cubes for removal of ionic dyes, J. Environ. Chem. Eng. 5 (1) (2017) 1096–1106.
[3] E. Alp, R. İmamoğlu, U. Savacı, S. Turan, M.K. Kazmanlı, A. Genç, Plasmon-enhanced photocatalytic and antibacterial activity of gold nanoparticles-decorated hematite nanostructures, J. Alloys Compd. 852 (2021) 157021.
[4] M. Yuan, M. Gong, H. Huang, Y. Zhao, Y. Ying, S. Wang, Bubble-propelled plasmon-reinforced Pt-ZnIn 2 S 4 micromotors for stirring-free photocatalytic water purification, Inorg. Chem. Front. (2022).
[5] J. Wu, D. Folio, J. Zhu, B. Jang, X. Chen, J. Feng, P. Gambardella, J. Sort, J. Puigmartí-Luis, O. Ergeneman, A. Ferreira, S. Pané, Motion analysis and real-time trajectory prediction of magnetically steerable catalytic janus micromotors, Adv. Intell. Syst. 4 (11) (2022) 2200192.
[6] T. Lei, C. Zhao, R. Yan, N. Zhao, Collective behavior of chiral active particles with anisotropic interactions in a confined space, Soft Matter 19 (7) (2023) 1312–1329.
[7] A. Xu, H.-L. Wu, H.-D. Xi, Long-distance migration with minimal energy consumption in a thermal turbulent environment, Phys. Rev. Fluids 8 (2) (2023) 023502.
[8] F. Cichos, K. Gustavsson, B. Mehlig, G. Volpe, Machine learning for active matter, Nat. Mach. Intell. 2 (2) (2020) 94–103.
[9] Z. Zhang, C. Boxall, G.H. Kelsall, Photoelectrophoresis of colloidal iron oxides 1. Hematite (α -Fe2O3), in: T.F. Tadros, J. Gregory (Eds.), Colloids in the Aquatic Environment, Elsevier, Oxford, 1993, pp. 145–163.
[10] S. Heckel, J. Hübner, A. Leutzgen, G. Jung, J. Simmchen, Progress report on pH-influenced photocatalysis for active motion, Catalysts 11 (5) (2021) 599.
[11] M. Wittmann, A. Ali, T. Gemming, F. Stavale, J. Simmchen, Semiconductor-based microswimmers: Attention to detail matters, J. Phys. Chem. Lett. 12 (39) (2021) 9651–9656.
[12] V. Sridhar, B.-W. Park, M. Sitti, Light-driven janus hollow mesoporous TiO2–Au microswimmers, Adv. Funct. Mater. 28 (25) (2018).
[13] G. Zhao, A. Ambrosi, M. Pumera, Self-propelled nanojets via template electrodeposition, Nanoscale 5 (4) (2013) 1319–1324.
[14] J. Palacci, S. Sacanna, S.-H. Kim, G.-R. Yi, D.J. Pine, P.M. Chaikin, Light-activated self-propelled colloids, Philos. Trans. Ser. A, Math. Phys. Eng. Sci. 372 (2029) (2014) 20130372.
[15] J. Palacci, S. Sacanna, A. Vatchinsky, P.M. Chaikin, D.J. Pine, Photoactivated colloidal dockers for cargo transportation, J. Am. Chem. Soc. 135 (43) (2013) 15978–15981.
[16] H. Massana-Cid, J. Codina, I. Pagonabarraga, P. Tierno, Active apolar doping determines routes to colloidal clusters and gels, Proc. Natl. Acad. Sci. USA 115 (42) (2018) 10618–10623.
[17] A. Aubret, Q. Martinet, J. Palacci, Metamachines of pluripotent colloids, Nat. Commun. 12 (1) (2021) 6398.
[18] J.M. Meijer, L. Rossi, Preparation, properties, and applications of magnetic hematite microparticles, Soft Matter 17 (9) (2021) 2354–2368.
[19] A.G. Tamirat, J. Rick, A.A. Dubale, W.-N. Su, B.-J. Hwang, Using hematite for photoelectrochemical water splitting: a review of current progress and challenges, Nanoscale Horizons 1 (4) (2016) 243–267.
[20] C. Kormann, D.W. Bahnemann, M.R. Hoffmann, Environmental photochemistry: Is iron oxide (hematite) an active photocatalyst? A comparative study: α -Fe2O3, ZnO, TiO2, J. Photochem. Photobiol. A: Chem. 48 (1) (1989) 161–169.
[21] P. Cendula, L. Steier, P.A. Losio, M. Grätzel, J.O. Schumacher, Analysis of optical losses in a photoelectrochemical cell: A tool for precise absorptance estimation, Adv. Funct. Mater. 28 (1) (2018).
[22] W.H. Leng, P.R.F. Barnes, M. Juozapavicius, B.C. O'Regan, J.R. Durrant, Electron diffusion length in mesoporous nanocrystalline TiO2 photoelectrodes during water oxidation, J. Phys. Chem. Lett. 1 (6) (2010) 967–972.
[23] K. Ozawa, M. Emori, S. Yamamoto, R. Yukawa, S. Yamamoto, R. Hobara, K. Fujikawa, H. Sakama, I. Matsuda, Electron–hole recombination time at TiO2 single-crystal surfaces: Influence of surface band bending, J. Phys. Chem. Lett. 5 (11) (2014) 1953–1957.
[24] S. Phromma, T. Wutikhun, P. Kasamechonchung, T. Eksangsri, C. Sapcharoenkun, Effect of calcination temperature on photocatalytic activity of synthesized TiO2 nanoparticles via wet ball milling sol-gel method, Appl. Sci. 10 (3) (2020) 993.
[25] S. Bharathi, D. Nataraj, D. Mangalaraj, Y. Masuda, K. Senthil, K. Yong, Highly mesoporous α -Fe2O3 nanostructures: preparation, characterization and improved photocatalytic performance towards Rhodamine B (RhB), J. Phys. D: Appl. Phys. 43 (1) (2009) 015501.
[26] X. Cui, T. Liu, Z. Zhang, L. Wang, S. Zuo, W. Zhu, Hematite nanorods with tunable porous structure: Facile hydrothermal-calcination route synthesis, optical and photocatalytic properties, Powder Technol. 266 (2014) 113–119.
[27] I. Mimouni, A. Bouziani, Y. Naciri, M. Boujnah, M.A. El Belghiti, M. El Azzouzi, Effect of heat treatment on the photocatalytic activity of α -Fe2O3 nanoparticles: towards diclofenac elimination, Environ. Sci. Pollut. Res. 29 (5) (2022) 7984–7996.
[28] J. Ding, Q. Zhong, S. Zhang, Catalytic efficiency of iron oxides in decomposition of H2O2 for simultaneous NOX and SO2 removal: Effect of calcination temperature, J. Mol. Catal. A: Chemical 393 (2014) 222–231.
[29] P. Zeng, Y. Zhao, Y. Lin, X. Wang, J. Li, W. Wang, Z. Fang, Enhancement of electrochemical performance by the oxygen vacancies in hematite as anode material for lithium-ion batteries, Nanoscale Res. Lett. 12 (1) (2017) 13.
[30] T. Sugimoto, K. Sakata, Preparation of monodisperse pseudocubic α -Fe2O3 particles from condensed ferric hydroxide gel, J. Colloid Interface Sci. 152 (2) (1992) 587–590.
[31] L. Rossi, S. Sacanna, W.T.M. Irvine, P.M. Chaikin, D.J. Pine, A.P. Philipse, Cubic crystals from cubic colloids, Soft Matter 7 (9) (2011) 4139–4142.
[32] S. Zevenhuizen, SPIEPy: SPIEPy (scanning probe image enchanter using python) is a python library to improve automatic processing of SPM images, 2023.
[33] O. Scholder, scholi/pySPM v0.2.20, 2019.
[34] S. Piccinin, The band structure and optical absorption of hematite (α -Fe2O3): a first-principles GW-BSE study, Phys. Chem. Chem. Phys. 21 (6) (2019) 2957–2967.
[35] S. Landi, I.R. Segundo, E. Freitas, M. Vasilevskiy, J. Carneiro, C.J. Tavares, Use and misuse of the Kubelka-Munk function to obtain the band gap energy from diffuse reflectance measurements, Solid State Commun. 341 (2022) 114573.
[36] J. Kieffer, V. Valls, deschila, T. Vincent, picca, payno, J. Wright, L. Huder, R. Pandolfi, G. Ashiotis, dodogerstlin, B. Faure, C.J.C. Wright, C. Weninger, gbenecke, jbhopkins, A. Hov, E. Prestat, G. Flucke, jangarrevoet, L. Märdian, mstorm, P. Hans, SigmundNeher, T.A. Caswell, woutdenolf, F. Plaswig, silx-kit/pyFAI: PyFAI v0.21.3, 2022.
[37] A.L. Patterson, The scherrer formula for X-ray particle size determination, Phys. Rev. 56 (10) (1939) 978–982.
[38] D.B. Allan, T. Caswell, N.C. Keim, C.M. van der Wel, R.W. Verweij, soft-matter/trackpy: Trackpy v0.5.0, 2021.
[39] J. Palacci, S. Sacanna, A.P. Steinberg, D.J. Pine, P.M. Chaikin, Living crystals of light-activated colloidal surfers, Science 339 (6122) (2013) 936–940.
[40] M. Ulfa, D. Prasetyoko, H. Bahruji, R.E. Nugraha, Green synthesis of hexagonal hematite (α -Fe2O3) flakes using pluronic F127-gelatin template for adsorption and photodegradation of ibuprofen, Materials 14 (22) (2021) 6779.
[41] E.N. Maslen, V.A. Streltsov, N.R. Streltsova, N. Ishizawa, Synchrotron X-ray study of the electron density in α -Fe2O3, Acta Crystallogr. Sect. B: Struct. Sci. 50 (4) (1994) 435–441.

[42] T. Sugimoto, A. Muramatsu, K. Sakata, D. Shindo, Characterization of hematite particles of different shapes, J. Colloid Interface Sci. 158 (2) (1993) 420–428.
[43] A.K. Patra, S.K. Kundu, A. Bhaumik, D. Kim, Morphology evolution of single-crystalline hematite nanocrystals: magnetically recoverable nanocatalysts for enhanced facet-driven photoredox activity, Nanoscale 8 (1) (2015) 365–377.
[44] D. Yuan, L. Zhang, J. Lai, L. Xie, B. Mao, D. Zhan, SECM evaluations of the crystal-facet-correlated photocatalytic activity of hematites for water splitting, Electrochem. Commun. 73 (2016) 29–32.
[45] Z. Li, J. Sheng, Y. Wang, Y. Xu, Enhanced photocatalytic activity and stability of alumina supported hematite for azo-dye degradation in aerated aqueous suspension, J. Hazard. Mater. 254–255 (2013) 18–25.
[46] Y. Wang, W. Du, Y. Xu, Effect of sintering temperature on the photocatalytic activities and stabilities of hematite and silica-dispersed hematite particles for organic degradation in aqueous suspensions, Langmuir 25 (5) (2009) 2895–2899.
[47] A.B.D. Nandiyanto, R. Zaen, R. Oktiani, Correlation between crystallite size and photocatalytic performance of micrometer-sized monoclinic WO3 particles, Arab. J. Chem. 13 (1) (2020) 1283–1296.
[48] J.R. Howse, R.A.L. Jones, A.J. Ryan, T. Gough, R. Vafabakhsh, R. Golestanian, Self-motile colloidal particles: From directed propulsion to random walk, Phys. Rev. Lett. 99 (4) (2007) 048102.
[49] C. Bechinger, R. Di Leonardo, H. Löwen, C. Reichhardt, G. Volpe, G. Volpe, Active particles in complex and crowded environments, Rev. Modern Phys. 88 (4) (2016) 045006.
[50] K. Goswami, A.G. Cherstvy, A. Godec, R. Metzler, Anomalous diffusion of active Brownian particles in responsive elastic gels: nonergodicity, non-Gaussianity, and distributions of trapping times, Phys. Rev. E: Stat. Phys. Plasmas, Fluids, Related Interdiscip. Top. 110 (4) (2024-10) 044609.
[51] M. Kaiser, S.S. Kantorovich, The importance of being a cube: Active cubes in a microchannel, J. Mol. Liq. 360 (2022) 119318.
[52] A.G. Cherstvy, S. Thapa, Y. Mardoukhi, A.V. Chechkin, R. Metzler, Time averages and their statistical variation for the ornstein-uhlenbeck process: role of initial particle distributions and relaxation to stationarity, Phys. Rev. E 98 (2) (2018-08-28) 022134.
[53] A.G. Cherstvy, W. Wang, R. Metzler, I.M. Sokolov, Inertia triggers nonergodicity of fractional Brownian motion, Phys. Rev. E 104 (2021) 024115.
[54] T.G. Mattos, C. Mejía-Monasterio, R. Metzler, G. Oshanin, First passages in bounded domains: when is the mean first passage time meaningful? Phys. Rev. E 86 (3) (2012-09-27) 031143.
[55] L. Rossi, J.G. Donaldson, J.-M. Meijer, A.V. Petukhov, D. Kleckner, S.S. Kantorovich, W.T.M. Irvine, A.P. Philipse, S. Sacanna, Self-organization in dipolar cube fluids constrained by competing anisotropies, Soft Matter 14 (7) (2018) 1080–1087.
[56] L. Wang, Y. Yu, H. He, Y. Zhang, X. Qin, B. Wang, Oxygen vacancy clusters essential for the catalytic activity of CeO2 nanocubes for o-xylene oxidation, Sci. Rep. 7 (1) (2017) 12845.
[57] S. Schyck, L. Rossi, Data for dissertation entitled “anisotropic and magnetic microparticles: preparation and out-of-equilibrium assembly”, 2023, http://dx.doi.org/10.4121/FE6B581D-6149-440D-8455-17CCE4E71F35.V1.